Supplementary Materials for "Depth-dependent azimuthal seismic anisotropy governed by Couette/Poiseuille flow partitioning in the asthenosphere"

Zhirui Ray Wang, Clinton P. Conrad, Sergei Lebedev, Giampiero Iaffaldano and John R. Hopper

This file contains:

- Supplementary text S1 and associated Figure S1
- Supplementary text S2 and associated Figures S2-S3
- Supplementary text S3 and associated Figures S4-S6
- Supplementary text S4 and associated Figure S7
- Supplementary text S5 and associated Figure S8
- Supplementary text S6 and associated Figure S9

S1. Geographical categorization of oceanic basins

Figure S1 shows the geographical categorization of the Pacific, Atlantic and Indian basins used in our study. Longitudes of 20°E, 130°E, and 72°W are used to subdivide these basins.

S2. Map views of azimuthal seismic anisotropy models

We present map views of the three azimuthal seismic anisotropy models utilized in this study. Our goal is to identify coherent anisotropy features

in all models, provided that they exploit different waveform datasets and modeling strategies. We choose three depth slices at 150, 200, and 250 km (Note that SL2016svA uses the depth slice at 260 km). Fig. S2 shows the orientations of azimuthal anisotropy at 150 km (orange sticks) and 200 km (cyan sticks). Background color denotes the directional difference between the two depth slices. We also show the scenarios that incorporate the cutoffs for associated peak-to-peak anisotropy amplitude (see main text). We plot the orientations at locations where their amplitudes meet the criterion at both depths. Fig. S3 displays the same inference as Fig. S2 except for 200 km (orange sticks) and 250 km (cyan sticks). We note that the orientations of azimuthal anisotropy and associated depth-rotations are broadly coherent under the Nazca plate. This holds in most scenarios, except for YB17SVaniSVD when the cutoff is above 0.5% at 200-250 km. This deviation is in part expected, since YB17SVaniSVD features a lower mean anisotropy amplitude under the Nazca plate than the other models (see Fig. 4d in main text).

S3. Depth rotation of azimuthal anisotropy models under various amplitude-cutoffs

Here we compute depth-rotation rates for azimuthal anisotropy models under various cutoffs for their peak-to-peak anisotropy amplitudes (i.e., 0.25%, 0.5%, and 0.75%). We recall that points that are below these cutoffs are excluded in our estimate. Figs. S4-S6a-i depict the results for individual oceanic domain. Overall, depth-rotation rates are prominent under the Atlantic basin in most scenarios, except for cutoff=0.75% (Fig. S6). We

attribute this to the relatively lower peak-to-peak amplitude measured under the Atlantic ocean (Fig. 4d in main text). Depth-rotation rates under the Nazca plate are also prominent in most cases (Figs. S4-S6j-l). Taken together, our analyses indicate that prominent depth rotations of azimuthal seismic anisotropy under the Atlantic basin and the Nazca plate are robust features.

S4. Impact of seismic anisotropy amplitude on inferred depth rotations above 200 km depth

Fig. S7 shows the impact of amplitude-cutoffs on inferred depth rotations above 200 km depth. In most cases, prominent depth rotations under the Atlantic basin and the Nazca plate are seen. This is consistent with similar calculations that extend to 300 km depth (Fig. 4 in the main text), and further supports the notion that depth rotation of azimuthal seismic anisotropy is a robust feature.

S5. Depth rotation of azimuthal seismic anisotropy inferred from YB17NAB

In this section, we estimate depth-rotation rates of azimuthal seismic anisotropy inferred from an alternate model YB17NAB (Yuan and Beghein, 2018). YB17NAB used a Bayesian framework (Sambridge, 1999a,b) to quantify its uncertainties and trade-offs of anisotropy model-parameters. We repeat the same procedure as done in the main text, except we only include points that are below an uncertainty provided by the model. Fig. S8 depict our results, where thresholds of uncertainty are 60°, 45°, and 30°. White

regions denote sections that are either (i) a part of oceanic lithosphere, or (ii) lacking as they do not meet the required threshold. Depth-rotations are less prominent beneath the Atlantic basin when uncertainties are below 60° (Fig. S8a). However, when uncertainty-thresholds are 45° and 30°, greater depth-rotations are seen under the Atlantic basin, especially above 200 km (Fig. S8b-c). This suggests that azimuthal seismic anisotropy, which implies prominent depth rotations under the Atlantic, contains relatively low uncertainty. In addition, depth-rotations under the Nazca plate weaken with a smaller threshold-uncertainty, in particular below 200 km (Fig. S8k,m,o) This could be due to the lack of points, where associated uncertainties satisfy the threshold.

S6. Impact of non-Newtonian rheology on the depth rotations of azimuthal seismic anisotropy

In this section, we test the effect of non-Newtonian, power-law rheology on the depth rotations of azimuthal seismic anisotropy. To do so, we built upon the formulations derived by Natarov and Conrad (2012) (see their section A3). For convenience of readers, we repeat the start of derivation from Natarov and Conrad (2012) by describing the relationship between stress τ and strain rate $\dot{\epsilon}$ as:

$$\tau = \frac{1}{C\tau_{II}^{n-1}}\dot{\epsilon} \tag{S1}$$

where C is a pre-exponential rheological factor, $1/(C\tau^{n-1})$ is the effective viscosity, τ_{II} is the second invariant of stress tensor, and n is the stress exponent. For the simplest case, we assume that shear terms are significant

only, and n=3, consistent with the dislocation creep in olivine (Karato and Wu, 1993). Hence:

$$\tau_{II}^2 = \tau_{13}^2 + \tau_{23}^2 \tag{S2}$$

Substituting Eq. S2 into Eq. S1 for both τ_{13} and τ_{23}:

$$\dot{\epsilon}_{13} = C(\tau_{13}^2 + \tau_{23}^2)\tau_{13} = \frac{du_1}{dx_3} \tag{S3a}$$

$$\dot{\epsilon}_{23} = C(\tau_{13}^2 + \tau_{23}^2)\tau_{23} = \frac{du_2}{dx_3} \tag{S3b}$$

where x_3 points upward along the asthenospheric depth. Here $\tau_{13} = C_1 + x_3\partial p/\partial x_1$ and $\tau_{23} = C_2 + x_3\partial p/\partial x_2$ based Eq. 1 of Natarov and Conrad (2012), and C_1 and C_2 are integration constants. Substituting the expressions of τ_{13} and τ_{23} into Eq. S3:

$$\frac{du_1}{dx_3} = C\left(\left(C_1 + \frac{\partial p}{\partial x_1}x_3\right)^2 + \left(C_2 + \frac{\partial p}{\partial x_2}x_3\right)^2\right)\left(C_1 + \frac{\partial p}{\partial x_1}x_3\right) \tag{S4a}$$

$$\frac{du_2}{dx_3} = C\left(\left(C_1 + \frac{\partial p}{\partial x_1}x_3\right)^2 + \left(C_2 + \frac{\partial p}{\partial x_2}x_3\right)^2\right)\left(C_2 + \frac{\partial p}{\partial x_2}x_3\right) \tag{S4b}$$

which is the same as Eq. A27 of Natarov and Conrad (2012). Here we assume the Couette and Poiseuille components are perpendicular to each other. In other words, the Couette and Poiseuille components orient along x_1 and x_2, respectively. In this case, $\partial p/\partial x_1$ vanishes, and Eq. S4 can be simplified as:

$$\frac{du_1}{dx_3} = C\left(C_1^2 + \left(C_2 + \frac{\partial p}{\partial x_2}x_3\right)^2\right)C_1 \tag{S5a}$$

$$\frac{du_2}{dx_3} = C\left(C_1^2 + \left(C_2 + \frac{\partial p}{\partial x_2}x_3\right)^2\right)\left(C_2 + \frac{\partial p}{\partial x_2}x_3\right) \tag{S5b}$$

Next we define the following dimensionless variables:

$$U_1 = \frac{u_1}{u_o} \tag{S6}$$

$$U_2 = \frac{u_2}{u_o} \tag{S7}$$

$$X_3 = \frac{x_3}{H} \tag{S8}$$

$$\alpha = \frac{CH^4}{u_o}|\nabla p|^3 \tag{S9}$$

$$\beta_{x_2} = \frac{\partial p}{\partial x_2}\frac{1}{|\nabla p|} \tag{S10}$$

$$C_{1n} = \frac{C_1}{|\nabla p|H} \tag{S11}$$

$$C_{2n} = \frac{C_2}{|\nabla p|H} \tag{S12}$$

where H is the asthenosphere thickness, u_o is the plate velocity, $|\nabla p|^2 = (\partial p/\partial x_1)^2 + (\partial p/\partial x_2)^2 = (\partial p/\partial x_2)^2$ in this case. Note that C_{1n} and C_{2n} are defined differently relative to the ones stated by Natarov and Conrad (2012) (C_1 and C_2 in their Eq. A28). Now substituting Eqs. S6-S12 into Eq. S5:

$$\frac{dU_1}{dX_3} = \alpha C_{1n}(C_{1n}^2 + (C_{2n} + \beta_{x_2} X_3)^2) \tag{S13a}$$

$$\frac{dU_2}{dX_3} = \alpha (C_{1n}^2 + (C_{2n} + \beta_{x_2} X_3)^2)(C_{2n} + \beta_{x_2} X_3) \tag{S13b}$$

Integrating Eqs. S13 with respect to X_3:

$$U_1 = \alpha C_{1n}(C_{1n}^2 X_3 + \frac{(C_{2n} + \beta_{x_2} X_3)^3}{3\beta_{x_2}}) + A \tag{S14a}$$

$$U_2 = \alpha (C_{1n}^2 C_{2n} X_3 + C_{1n}^2 \beta_{x_2} \frac{X_3^2}{2} + \frac{(C_{2n} + \beta_{x_2} X_3)^4}{4\beta_{x_2}}) + B \tag{S14b}$$

where A and B are integration constants. Next we apply boundary conditions $U_1(0) = 1$, $U_1(-1) = 0$, $U_2(0) = 0$, and $U_2(-1) = 0$. This gives us following expressions:

$$A = 1 - \alpha C_{1n} \frac{C_{2n}^3}{3\beta_{x_2}} \tag{S15}$$

$$0 = -\alpha C_{1n}^3 + 1 + \frac{\alpha C_{1n}}{3\beta_{x_2}}((C_{2n} - \beta_{x_2})^3 - C_{2n}^3) \tag{S16}$$

$$B = -\frac{\alpha C_{2n}^4}{4\beta_{x_2}} \tag{S17}$$

$$0 = -C_{1n}^2 C_{2n} \alpha + \frac{\alpha C_{1n}^2 \beta_{x_2}}{2} + \frac{\alpha}{4\beta_{x_2}}((C_{2n} - \beta_{x_2})^4 - C_{2n}^4) \tag{S18}$$

Eqs. S15-S18 need to be solved numerically in order to determine A, B, C_{1n}, and C_{2n}. Here one needs to determine the dimensionless velocity gradient along x_1 and x_2 (Eq. S13), followed by the associated strain-axis

orientation, which can be treated as a proxy for LPO over depth. For conceptual purposes, we test three input $|\nabla p|$ (i.e., 1, 2, and 5 Pa/m), while keeping the remaining dimensionless variables as 1. In addition, we use Eq. 8 from Natarov and Conrad (2012) to compute the strain-axis orientation with a Newtonian setting for comparisons.

Fig. S9 shows the resulting dimensionless flow profiles for the Couette (left column) and Poiseuille (middle column) components, as well as the orientations of strain axis (right column). Solid and dashed curves denote non-Newtonian and Newtonian cases, respectively. In the non-Newtonian setting that features power-law rheology, viscosity near the top and bottom of asthenosphere would be reduced due to the Poiseuille flow gradients. This viscosity change would affect behaviors of both Couette and Poiseuille flows. For smaller lateral pressure gradients (e.g., 1 & 2 Pa/m), velocity profiles of the Couette and Poiseuille components are broadly similar between Newtonian and non-Newtonian settings, and their strain axis orientations exhibit negligible differences (Fig. S9a-e). For a larger lateral pressure gradient (e.g., 5 Pa/m), Poiseuille flow manifests as "plug flow" (Semple and Lenardic (2018); Ramirez et al. (2023)) with greater velocity magnitudes in the non-Newtonian case (Fig. S9h), while the Couette component exhibits a sigmoidal behavior (Fig. S9h). This leads to a larger depth rotation of the strain axis, especially near mid-asthenosphere (Fig. S9i). However, as stated in the main manuscript, we speculate that this effect will not significantly affect the regional dependence on depth rotations, since they are tied to the relative importance of the Couette and Poiseuille components.

References

Karato, S.i., Wu, P., 1993. Rheology of the upper mantle: A synthesis. Science 260, 771–778. doi:https://doi.org/10.1126/science.260.5109.771.

Natarov, S.I., Conrad, C.P., 2012. The role of Poiseuille flow in creating depth-variation of asthenospheric shear. Geophysical Journal International 190, 1297–1310. doi:https://doi.org/10.1111/j.1365-246X.2012.05562.x.

Ramirez, F.D., Conrad, C.P., Selway, K., 2023. Grain size reduction by plug flow in the wet oceanic upper mantle explains the asthenosphere's low seismic Q zone. Earth and Planetary Science Letters 616, 118232. doi:https://doi.org/10.1016/j.epsl.2023.118232.

Sambridge, M., 1999a. Geophysical inversion with a neighbourhood algorithm—I. Searching a parameter space. Geophysical Journal International 138, 479–494. doi:https://doi.org/10.1046/j.1365-246X.1999.00876.x.

Sambridge, M., 1999b. Geophysical inversion with a neighbourhood algorithm—II. Appraising the ensemble. Geophysical Journal International 138, 727–746. doi:https://doi.org/10.1046/j.1365-246x.1999.00900.x.

Semple, A.G., Lenardic, A., 2018. Plug flow in the Earth's asthenosphere. Earth and Planetary Science Letters 496, 29–36. doi:https://doi.org/10.1016/j.epsl.2018.05.030.

Yuan, K., Beghein, C., 2018. A Bayesian method to quantify azimuthal anisotropy model uncertainties: application to global azimuthal anisotropy in the upper mantle and transition zone. Geophysical Journal International 213, 603–622. doi:https://doi.org/10.1093/gji/ggy004.

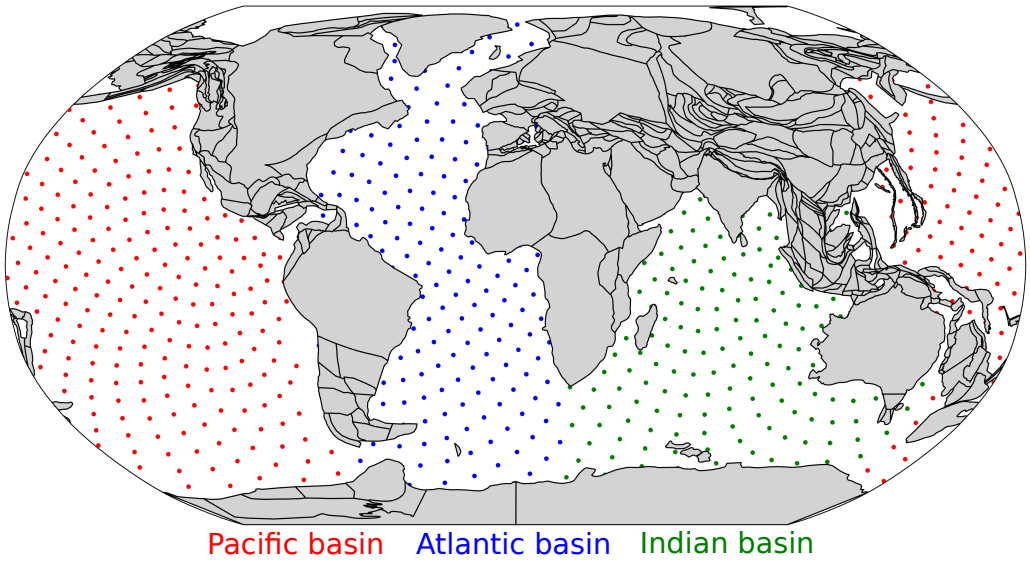

Figure S1: Geographical categorization for Pacific (red), Atlantic (blue) and Indian (green) basins using 1000 points over a fibonacci sphere.

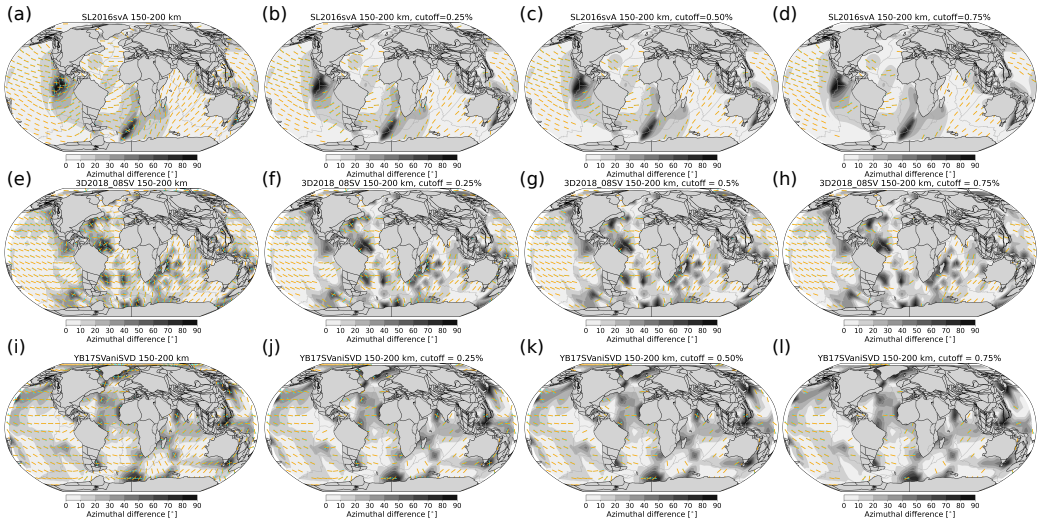

Figure S2: Map views of azimuthal seismic anisotropy under the oceans for SL2016SVa (a-d), 3D2018_08SV (e-h), and YB17SVaniSVD (i-l) at 150 km (orange) and 200 km (cyan). Background color denotes the directional difference of azimuhtal anisotropy between two depths. For scenarios that incorporate cutoffs for peak-to-peak anisotropy amplitudes, we only show the azimuthal anisotropy that satisfies the cutoffs at both depths.

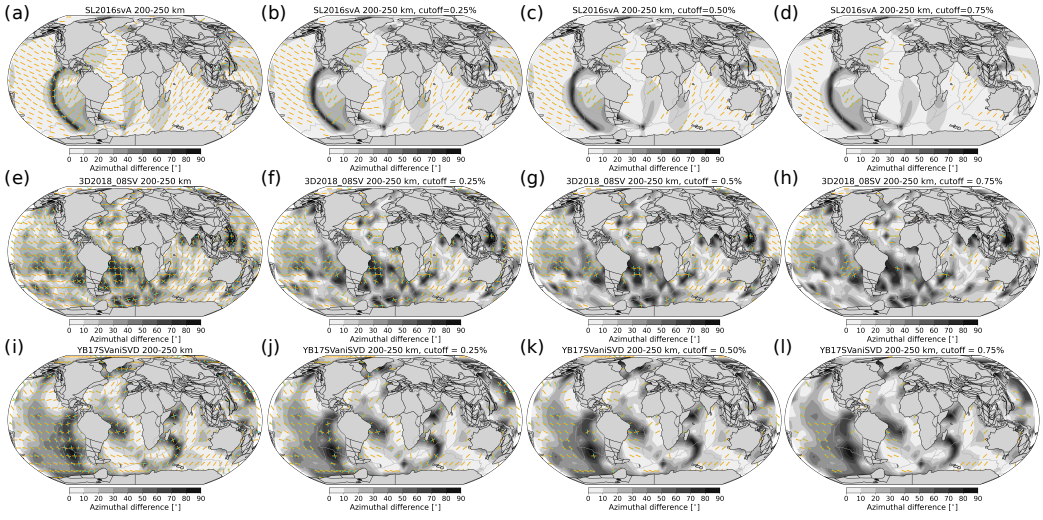

Figure S3: Same as Fig. S2, except for azimuthal seismic anisotropy at 200 km (orange) and 250 km (cyan).

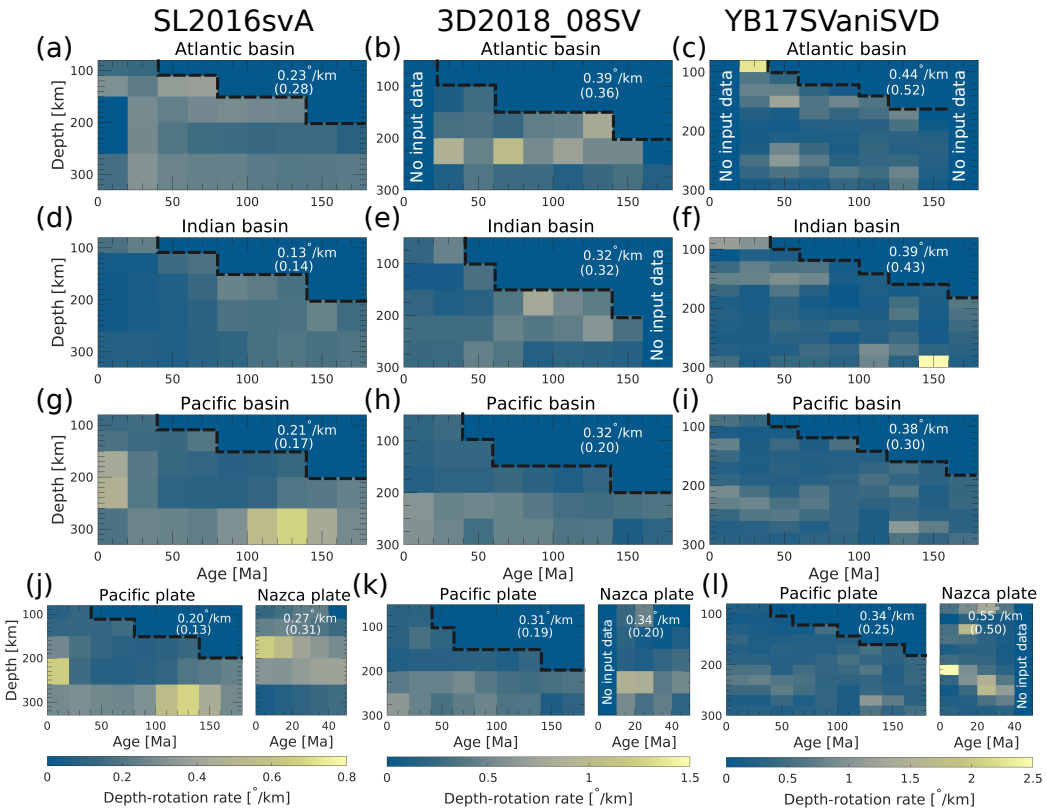

Figure S4: Depth-rotation rate of azimuthal seismic anisotropy as a function of ocean-floor age and depth under individual oceanic basins (a-i), as well as the Pacific and Nazca plates (j-l), using an amplitude-cutoff of 0.25%. Color-coding and notations are same as Fig. 3 in the main manuscript.

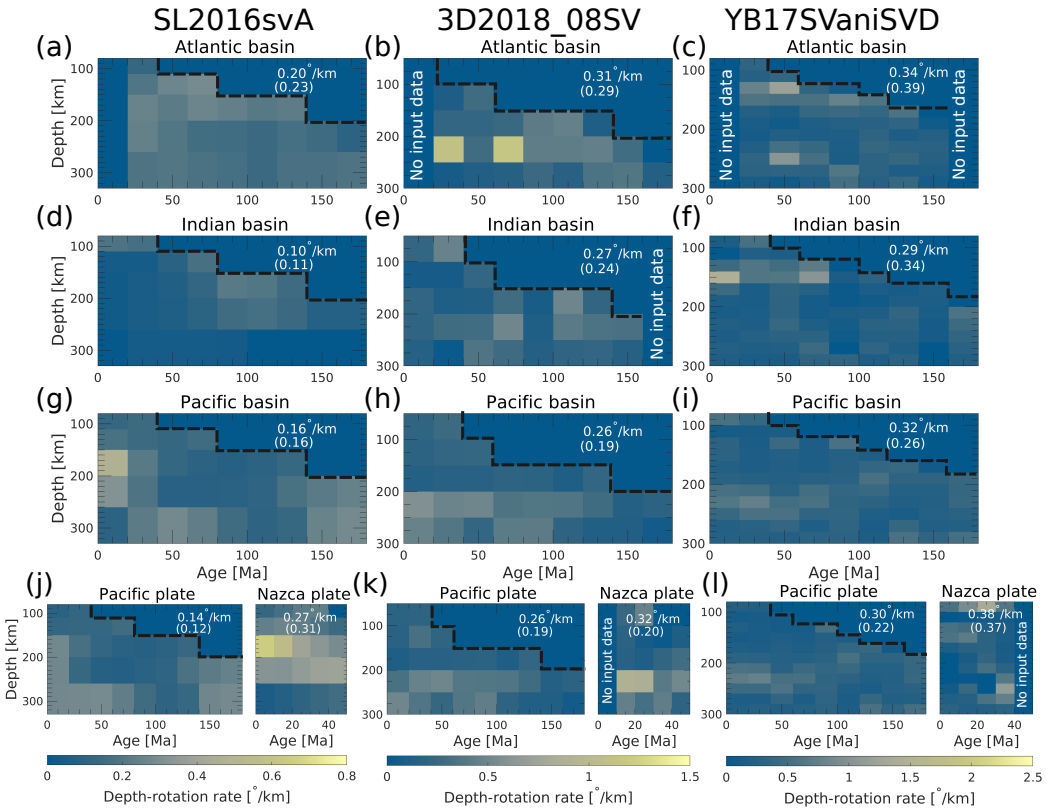

Figure S5: Same as Fig. S4, except using an amplitude-cutoff of 0.5%. Color-coding and notations are same as Fig. 3 in the main manuscript.

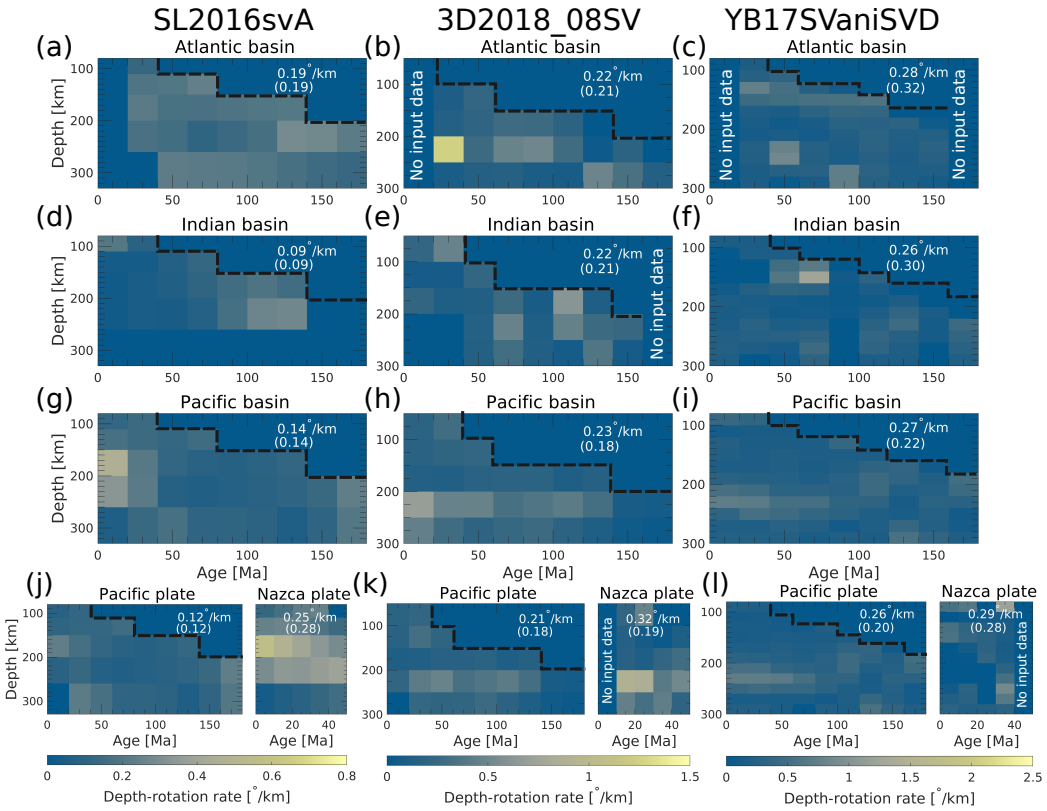

Figure S6: Same as Fig. S4, except using an amplitude-cutoff of 0.75%. Color-coding and notations are same as Fig. 3 in the main manuscript.

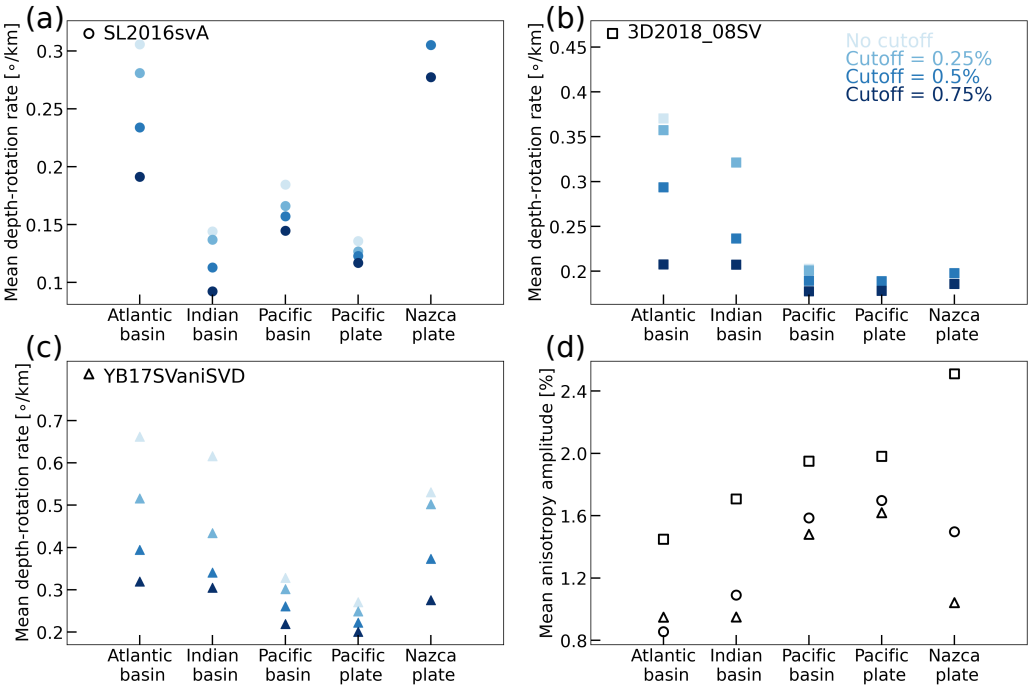

Figure S7: Same as Fig. 4 in the main manuscript, except the calculations are done for grid points above 200 km depth.

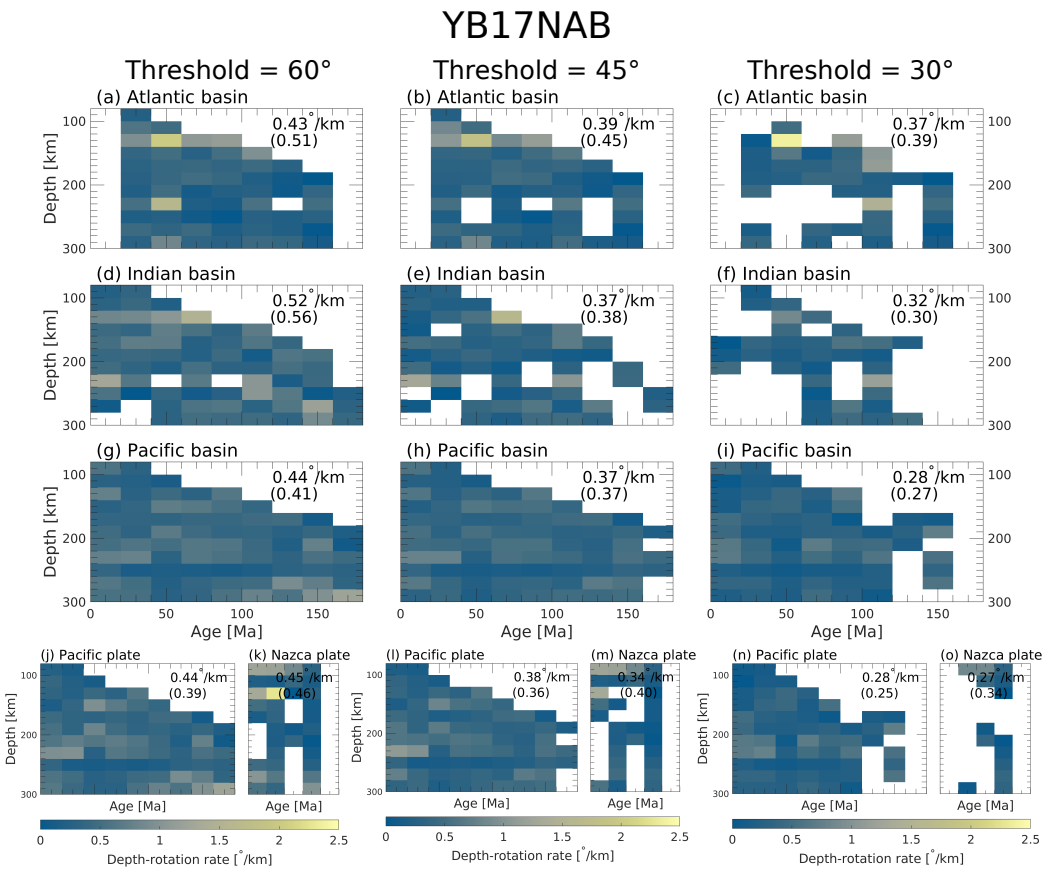

Figure S8: Depth-rotation rate for the model YB17NAB (Yuan and Beghein, 2018) as a function of depth and ocean-floor age. Depth-rotation rates are computed with points that are below the given uncertainties of 60° (left), 45° (middle), and 30° (right). White regions indicate sections where inferred azimuthal seismic anisotropy is either (i) within the oceanic lithosphere, or (ii) lacking because it exceeds the uncertainty-thresholds. The remaining color-coding and notations are same as for Fig. 3 in the main manuscript.

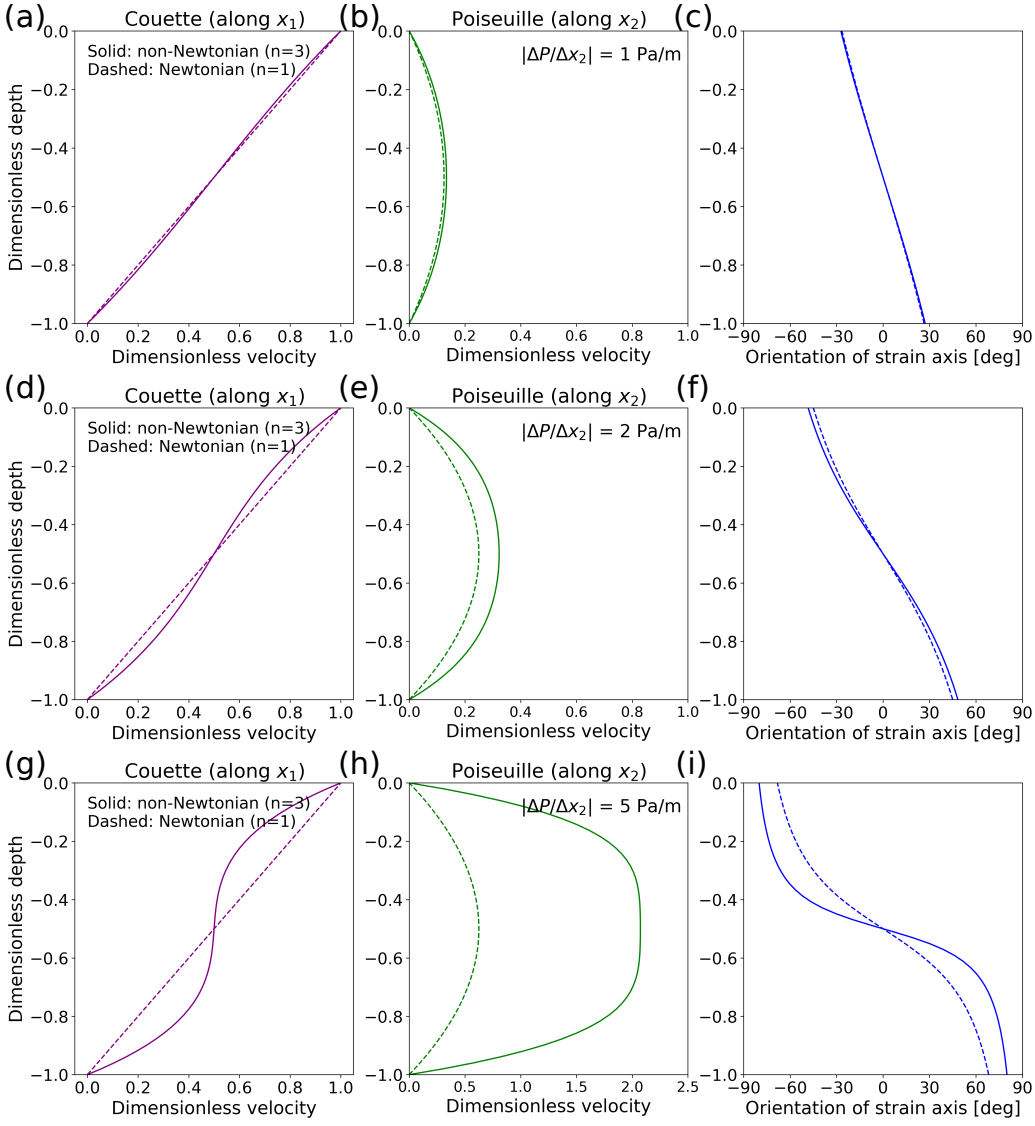

Figure S9: Dimensionless velocity profiles for the Couette (along x_1; left column) and Poiseuille (along x_2; middle column) components, as well as the resulting orientations of the strain axis from their combined flow fields (right column). Three different dimensional lateral pressure gradients are used as an input: 1 Pa/m (a-c), 2 Pa/m (d-f), and 5 Pa/m (g-l). Solid and dashed curves denote non-Newtonian (stress component n=3), and Newtonian (n=1) settings, respectively.